

Electronic structure based descriptor for characterizing local atomic environmentsJan Jenke,¹ Aparna P. A. Subramanyam,¹ Marc Densow,¹ Thomas Hammerschmidt,¹ David G. Pettifor,² and Ralf Drautz¹¹ICAMS, Ruhr-Universität Bochum, D-44801 Bochum, Germany²Department of Materials, University of Oxford, Oxford OX1 3PH, United Kingdom

(Received 21 December 2017; revised manuscript received 24 July 2018; published 3 October 2018)

A quantitative descriptor of local atomic environments is often required for the analysis of atomistic data. Descriptors of the local atomic environment ideally provide physically and chemically intuitive insight. This requires descriptors that are low-dimensional representations of the interplay between atomic geometry and electronic bond formation. The moments of the local density of states relate the atomic structure to the electronic structure and bond chemistry. This makes it possible to construct electronic structure based descriptors of the local atomic environment that have an immediate relation to the binding energy. We show that a low-dimensional moments-descriptor is sufficient as the lowest moments, calculated from the closest atomic neighborhood, carry the largest contributions to the local bond energy. Here, we construct moments-descriptors that project the space of local atomic environments on a two-dimensional map. We discuss in detail the separation of various atomic environments and their connections in the map. The distances in the map may be related to energy differences between local atomic environments as we show by analytic considerations based on analytic bond-order potentials and by numerical assessment using tight-binding and density-functional theory calculations. Possible applications of the proposed moments-descriptors include the classification of local atomic environments in molecular-dynamic simulations, the selection of structure sets for developing and testing interatomic potentials, as well as the construction of descriptors for machine-learning applications.

DOI: [10.1103/PhysRevB.98.144102](https://doi.org/10.1103/PhysRevB.98.144102)**I. INTRODUCTION**

Descriptors are frequently employed in the statistical analysis of physical and chemical properties of materials. For example, local bond-order parameters are used in structure identification [1,2], parametrizations of interatomic interactions utilize the bispectrum [3], smooth overlaps of atomic positions [4], or atom-centered symmetry functions [5–7], to name just a few. Molecular properties are predicted based on the Coulomb matrix [8], Fourier series of atomic radial distribution functions [9], and the bag of bonds method [10]. Materials properties are evaluated from combinations of atomic quantities [11–13], partial radial distribution functions [14], or structural and electronic fingerprints [15]. Descriptors are further used in the classification of structural properties in structure maps [11] and property maps [12,13,15].

Here we show that the moments of the density of states (DOS) may serve as robust descriptors of the local atomic structure that allow for an intuitive grouping and classification of atomic environments in a map. The local electronic DOS intimately relates the energy on the one hand to the atomic structure on the other hand. The formal relation between the moments of the DOS and the local crystal structure was introduced explicitly with the moments theorem [16]. The moments theorem enables the computation of the moments of the local DOS without the computationally expensive calculation of the eigenspectrum and is used for linear scaling expansions of the band energy [17–26] and more recently also to define difference vectors between pairs of crystal structures [27]. Moments-based expansions exploit that in general the lowest moments of the DOS have the largest contribution

to the cohesive energy [25,26] and therefore are, together with geometrical constraints, critical in the determination of low-energy atomic environments.

In the present paper, we exploit the fact that the lowest moments have in general the largest contribution to the energy, which allows us to project the space of atomic environments on a two-dimensional (2D) map. The 2D map of local atomic environments can be sampled with high-throughput density functional theory (DFT) calculations and may be employed for scanning local atomic environments, for example for the selection of crystal structures for testing or developing interatomic potentials, the separation or classification of crystal structures, and the comparison of existing descriptors in a low-dimensional space. The paper is organized as follows. In Sec. II we introduce the moments of the density of states and discuss how they may serve as descriptors. This allows us to set up a 2D map of local atomic environments in Sec. III. In Sec. IV we relate structural energy differences in the map to differences in structural stability obtained by tight-binding (TB) and DFT calculations. In Sec. V an outlook on possible applications of the map of local atomic environments and the moments-descriptors is given, and in Sec. VI we conclude our findings.

II. MOMENTS-DESCRIPTORS

In electronic structure calculations such as DFT or TB, the electronic DOS is usually obtained by diagonalizing the Hamiltonian \hat{H} . The Hamiltonian thereby contains the complete information required for characterizing the electronic structure of a material and depends in particular on the

positions of the atoms as well as their chemistry. Therefore, the moments of the DOS incorporate information on the atomic structure as well as the chemistry of a material. The moments of the DOS are explicitly linked to the crystal structure and chemistry through the moments theorem. We summarize the moments theorem [16] for a local, orthonormal set of basis functions. The N th moment of the local DOS $n_{inlm}(E)$ of orbital n with angular momentum l and projection m on atom i is defined by

$$\mu_{inlm}^{(N)} = \int_{-\infty}^{\infty} E^N n_{inlm}(E) dE, \quad (1)$$

with the energy E . The moments theorem states that the N th moment of the local DOS can be computed by summing over all self-returning paths of Hamiltonian matrix elements of length N that start and end at orbital $inlm$,

$$\begin{aligned} \mu_{inlm}^{(N)} = & \sum_{\substack{i_1 n_1 l_1 m_1, \\ i_2 n_2 l_2 m_2, \dots}} \langle inlm | \hat{H} | i_1 n_1 l_1 m_1 \rangle \\ & \times \langle i_1 n_1 l_1 m_1 | \hat{H} | i_2 n_2 l_2 m_2 \rangle \\ & \times \langle i_2 n_2 l_2 m_2 | \hat{H} | \dots \rangle \dots \langle \dots | \hat{H} | inlm \rangle. \end{aligned} \quad (2)$$

By averaging contributions of different magnetic quantum numbers, rotationally invariant atomic moments are obtained,

$$\mu_{inl}^{(N)} = \frac{1}{2l+1} \sum_{m=-l}^{+l} \mu_{inlm}^{(N)}. \quad (3)$$

The atomic moments are by construction also invariant with respect to reflection, translation of the atomic structure, and to permutation of atoms of the same species, and they fulfill the basic requirements for an atomic scale descriptor [4,5].

As the DOS is strictly positive, we may normalize the zeroth moment to 1, $\mu_{inl}^{(0)} = 1$. The first moment corresponds to the center of gravity of the DOS,

$$\mu_{inl}^{(1)} = E_{inl}. \quad (4)$$

By an appropriate shift $E \rightarrow E - E_{inl}$ of the energy scale, we achieve $\mu_{inl}^{(1)} = 0$. The second moment, the root-mean-square width of the local DOS, is the lowest moment that depends on the atomic environment,

$$\begin{aligned} \mu_{inl}^{(2)} = & \frac{1}{2l+1} \sum_{mi'n'l'm'} \langle inlm | \hat{H} | i'n'l'm' \rangle \\ & \times \langle i'n'l'm' | \hat{H} | inlm \rangle. \end{aligned} \quad (5)$$

Through the dependence of the second moment on the Hamiltonian matrix, the second moment depends explicitly on the interatomic distances. As our focus is on the characterization of local atomic environments without an explicit scaling length or density dependence, we need to remove the distance dependence from the second moment. This is achieved by homogeneously scaling interatomic distances such that

$$\mu_{inl}^{(2)} = 1. \quad (6)$$

With the above scaling, the third and fourth moments $\mu_{inl}^{(3)}$ and $\mu_{inl}^{(4)}$ (that contribute information on the skewness and

bimodality of the local DOS) are the lowest two moments that depend explicitly on the local atomic structure.

Instead of working with the third and fourth moments directly, we rewrite the moments in the form of recursion coefficients [28]. The recursion coefficients are the matrix elements of a Hamiltonian that is transformed onto a 1D semi-infinite chain. With the normalization $\mu^{(0)} = 1$, $\mu^{(1)} = 0$, and $\mu^{(2)} = 1$, the corresponding recursion coefficients are given by

$$a^{(1)} = \mu^{(3)}, \quad (7)$$

$$b^{(2)} = \sqrt{\mu^{(4)} - (\mu^{(3)})^2 - 1}, \quad (8)$$

with the common index inl omitted. The recursion coefficients $a^{(1)}$ and $b^{(2)}$ are the two moments-descriptors that we use to span the map of local atomic environments. The recursion coefficient $a^{(1)}$ measures the skewness of the local DOS, while the recursion coefficient $b^{(2)}$ is a dimensionless shape parameter [29], which is smaller than 1 for a bimodal local DOS and larger than 1 for a unimodal DOS.

The recursion coefficients are independent parameters that may in principle attain independently any value for $a^{(1)}$ or any positive value for $b^{(2)}$. This is not true for the moments that are not independent. For example, from $(b^{(2)})^2 \geq 0$ we immediately obtain

$$\mu^{(4)} \geq (\mu^{(3)})^2 + 1. \quad (9)$$

Inequalities for higher moments can also be derived [30].

For the computation of the moments-descriptors $a^{(1)}$ and $b^{(2)}$ for a particular atomic structure, a Hamiltonian \hat{H} is required in the evaluation of Eq. (1). While this Hamiltonian could be taken from DFT, we focus on obtaining a map of local atomic environments that may be used for different materials. We achieve this by using model TB Hamiltonians [Eqs. (A1) and (A2)] that show good transferability across the transition metals and the sp -elements, respectively [31,32]. These simple models of the bonding chemistry enable us to analyze the influence of valence character and band filling on the binding energy and the resulting structural stability. Details of the TB models are summarized in Appendix A. In addition, the choice of a TB model allows for an efficient calculation of the moments of the local DOS of atom i by Eq. (2) without computation of the TB eigenspectrum. The numerical calculation of moments and recursion coefficients in this work was performed with the BOPFOX program [33].

III. MAP OF LOCAL ATOMIC ENVIRONMENTS

We will next introduce the map of local atomic environments and illustrate its efficiency for separating crystal structures. We will further motivate the descriptors by relating them to the binding energy in Sec. IV. Figure 1 shows the d -valent map of local atomic environments that is spanned by $a^{(1)}$ and $b^{(2)}$, which are computed with the d -valent TB model. The red filled circles correspond to crystal structures with only one atomic environment. Other symbols indicate the differently coordinated atoms in more complex crystal structures. Furthermore, existence regions for structures with one, two, or more inequivalent atoms are marked as patterned areas

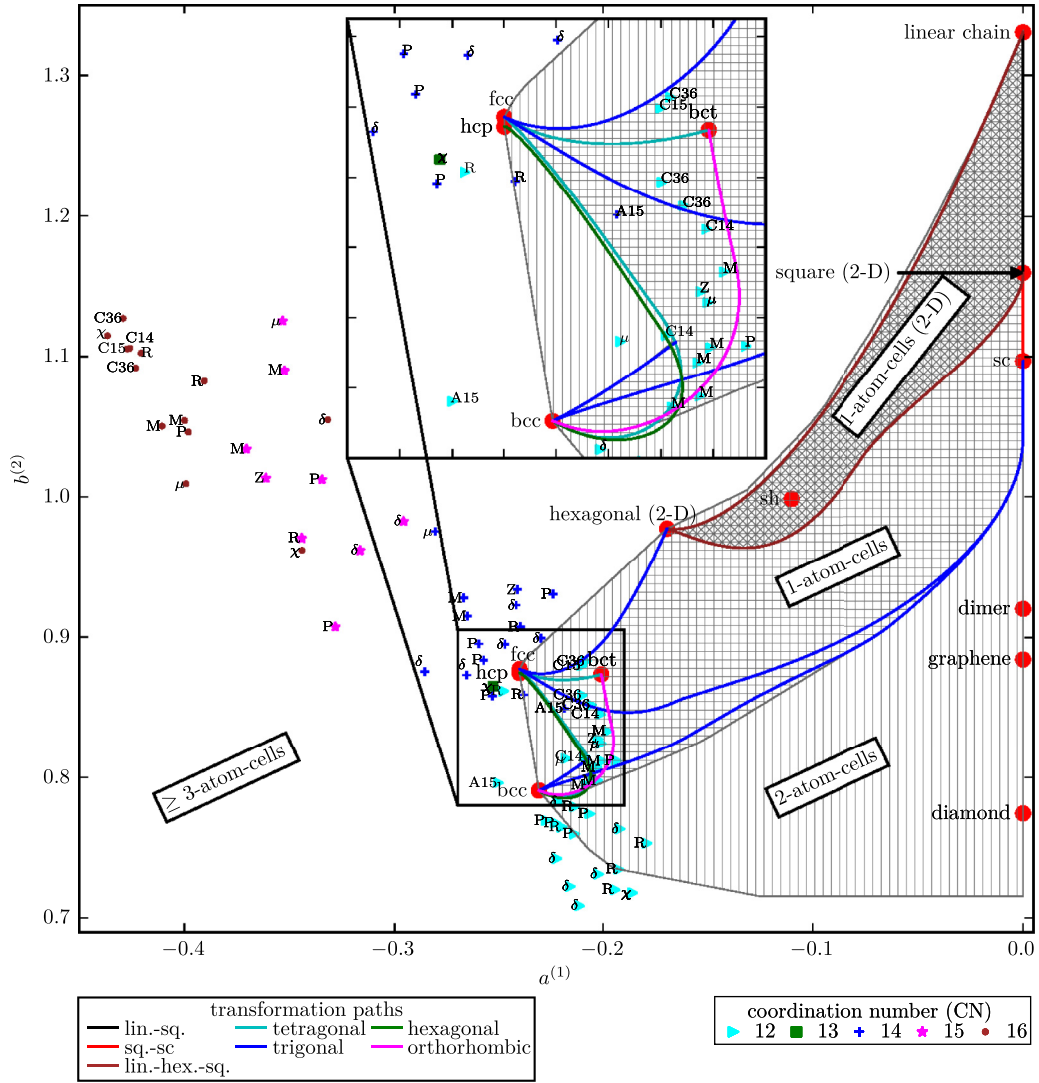


FIG. 1. Map of local atomic environments for a d -valent Hamiltonian. Depicted are different crystal structures, transformation paths, and estimated envelopes that demarcate the regions in which crystal structures with one, two, or more inequivalent atoms may exist. Red filled circles correspond to crystal structures with only one atomic environment. Additional symbols indicate the position of differently coordinated atoms in more complex crystal structures; the common names for TCP phases are given next to the symbols. A square pattern shows the region into which all structures with only one atom in the primitive cell fall. The region of 2D one-atom structures is further marked by diagonal lines. The existence region of crystal structures that contain a maximum of two atoms in the primitive cell is indicated by vertical lines. This region includes the region of one-atom cells. Crystal structures with three or more atoms in the primitive cell can in principle reach any position in the map. Transformation paths between different crystal structures are shown using colored lines. The region around the close-packed phases (bcc, fcc, hcp) is magnified.

while transformation pathways between different structures are shown as lines. The envelopes of the existence regions are estimated from the positions of a large set of random structures (cf. Sec. III C).

A. Simple crystal structures

The map of local atomic environments provides a clear separation of simple crystal structures with only one atomic environment (filled red circles). For the linear chain (linear), the 2D square lattice (square 2D), and the simple-cubic (sc) structure, graphene, and diamond, the third moment is zero. They are therefore placed on the line $a^{(1)} = 0$ on the right of the map. The linear chain, the 2D square lattice, and the

simple-cubic structure are ordered according to their dimensionality. They are followed by the dimer, graphene, and diamond. The dimer, graphene, and diamond have characteristically lower values of $b^{(2)}$, which leads to their stabilization in some materials, as we will discuss in Sec. IV B.

Toward the left of the map of local atomic environments we find the close-packed structures face-centered cubic (fcc), hexagonal close-packed (hcp), and body-centered cubic (bcc). The map of local atomic environments places fcc and hcp, which typically have a very similar cohesive energy, almost on top of each other. The values of the moments-descriptors differ only due to their small fourth moment contributions [25]. The small difference is a result of the different stacking sequence of ABC for fcc and ABA for hcp, which has a small

effect on the self-returning paths that reach the third layer [34].

Among the simple structures, the map places the bcc structure next to fcc and hcp. Once more this is intuitive as the three structures are realized in transition-metal elements. The special body-centered-tetragonal (bct) [35] structure is close to the close-packed structures. Between the close-packed structures and the open structures with $a^{(1)} = 0$ are the simple-hexagonal and body-centered-tetragonal structure as well as the 2D close-packed hexagonal lattice (2D hexagonal).

By construction the positions in the map of local atomic environments may be related to the local density of states of the different crystal structures: The linear chain, the 2D square lattice, the simple-cubic structure, the dimer, graphene, and diamond all have a symmetric DOS ($\mu^{(3)} = 0$). The dimer, which has a perfect bimodal DOS ($b^{(2)} = 0$) for s -orbitals, shows a finite value of $b^{(2)}$ for d -orbitals, and the DOS of graphene and diamond are even more bimodal. The 2D hexagonal lattice has the most skewed DOS among the 2D structures with one atom in the primitive cell. The bcc structure is more bimodal and less skewed than fcc and hcp [25].

Some of the simple crystal structures are related by structural transformation paths that can readily be included in the map of local atomic environments (cf. Fig. 1). More details on the different transformation paths are compiled in Appendix B. All transformation paths starting from the close-packed structures initially go to the right in the map of local atomic environments. The two transformation paths lin.-sq. and lin.-hex.-sq. form a closed area. This area is in agreement with the estimated envelope of the 2D structures with one atom in the primitive cell. The trigonal transformation path connects bcc with the simple-cubic structures. The tetragonal transformation path from bcc to fcc is almost on top of the hexagonal transformation from bcc to hcp indicating that the intermediate structures along both paths are similar to each other. After approaching fcc, the tetragonal transformation path abruptly changes its direction toward the special bct structure. This structure is also reached by the orthorhombic transformation [35]. The orthorhombic path returns from bct to bcc along the same path as from bcc to bct. The trigonal path, the tetragonal path, and the lin.-hex. path also form parts of the envelope for 3D structures with one atom in the primitive cell.

B. Crystal structures with multiple inequivalent lattice sites

For structures with several inequivalent atomic environments, a symbol is displayed in the map for each atomic environment. We show the different atomic environments of topologically close-packed (TCP) phases that are briefly introduced in Appendix C. The moments of the DOS have been applied to quantify the difference between TCP phases and to identify trends of the local moments with coordination number [27,36,37]. The 12-fold coordinated atoms in the TCP phases are close to the fcc and hcp structures in the map. For atoms with higher coordination, the absolute values of $a^{(1)}$ and $b^{(2)}$ increase. The sublattices of the χ -phase also follow this trend; the 13-fold coordinated site is close to the hcp structure. We observe a clear trend of coordination in the map of local atomic environments (see Fig. 1): Atoms with similar

coordination numbers are close to each other, but still can be distinguished in the map of local atomic environments. Atoms with high coordination leave the region of simple structures with one or two atoms in the primitive cells, indicating that these atomic environments can only occur in combination with lattice sites of lower coordination.

C. Random structures

We furthermore use randomly generated structures to evaluate domains in the map of local atomic environments that may be covered by structures with one or two atoms in the primitive cell. Details on the construction of the random structures are given in Appendix D. The domain of structures with one-atom cells is surprisingly small. It covers the region from the linear chain and the simple-cubic lattice at $a^{(1)} = 0$ to the close-packed bcc and fcc phases. A significant area of the domain corresponds to 2D structures. For two atoms in the primitive cell, the one-atom domain is expanded significantly to lower values of $b^{(2)}$ and comprises the dimer, graphene, and diamond structures. Crystal structures with three or more atoms in the cell can in principle reach any point in the map. Figure 1 also shows that the transformation paths between simple structures provide envelopes of 2D and 3D structures with one atom in the primitive cell.

IV. ELECTRONIC STRUCTURE INTERPRETATION OF MOMENTS-DESCRIPTORS

A. Relation of moments-descriptors to binding energy

We rationalize structural stability across the maps of local atomic environments by a TB model. We do not account for charge transfer between atoms or between different orbitals within an atom (i.e., the promotion energy) or magnetism. With these approximations, the energy may be written as [38,39]

$$U = U_{\text{bond}} + U_{\text{rep}}. \quad (10)$$

To lowest order the repulsive contribution may be assumed to be pairwise [38,39],

$$U_{\text{rep}} = \frac{1}{2} \sum_{ij} \Phi_{ij}(r_{ij}). \quad (11)$$

It is possible to estimate the energy difference between two structures without explicit parametrization of the repulsive contribution to the energy by making use of the structural energy difference theorem [40]: if two structures are compared at identical repulsive energy, the energy difference between the two structures is given to first order by the difference in bond energy,

$$\Delta U \approx [\Delta U_{\text{bond}}]_{\Delta U_{\text{rep}}=0}. \quad (12)$$

For computing ΔU one can in many cases [41] assume that U_{rep} is dominated by the overlap repulsion [29,37,42]

$$\Phi_{ij}(r) \propto \beta^2(r), \quad (13)$$

where the distance dependence of $\beta(r)$ is proportional to the distance dependence of the Hamiltonian matrix elements. From Eq. (5) it then follows that the second moment is

proportional to the atomic repulsion,

$$\mu^{(2)} \propto \sum_j \frac{1}{2} \Phi_{ij}. \quad (14)$$

By requiring that all structures in the map of local atomic environments have identical second moments, Eq. (6), the energy difference between two structures may be estimated from the bond energy difference ΔU_{bond} .

The atomic bond energy may be obtained from integrating the density of states up to the Fermi level E_F ,

$$U_{\text{bond},i} = \int^{E_F} (E - E_i) n_i(E) dE. \quad (15)$$

The analytic bond-order potentials (BOP) provide an expansion of the bond energy in terms of its moments and the Fermi energy [25,26],

$$U_{\text{bond},i} = 2(2l+1)b^{(\infty)} \left\{ \sum_{m=0}^{n_{\text{max}}} \sigma_i^{(m)} [\hat{\chi}_{m+2}(\phi_F) - \gamma_0 \hat{\chi}_{m+1}(\phi_F) + \hat{\chi}_m(\phi_F)] \right\}, \quad (16)$$

where $b^{(\infty)}$ scales the energy range of the density of states to the interval $\epsilon = [-1, 1]$. The expansion coefficients are given by the Chebyshev moments of the density of states,

$$\sigma_i^{(m)} = \int_{-1}^1 U_m(\epsilon) n_i(\epsilon) d\epsilon, \quad (17)$$

with the Chebyshev polynomials of the second kind U_m , and they may therefore be obtained from the moments of the density of states; cf. Eq.(1).

The response functions $\hat{\chi}_n$ depend on ϕ_F , which is defined by the Fermi energy $E_F = a^{(\infty)} + 2b^{(\infty)} \cos \phi_F$, where $a^{(\infty)}$ is the center of the band, $\gamma_0 = (\mu^{(1)} - a^{(\infty)})/(2b^{(\infty)})$, and

$$\hat{\chi}_1(\phi_F) = 1 - \frac{\phi_F}{\pi} + \frac{1}{2\pi} \sin(2\phi_F), \quad (18)$$

$$\hat{\chi}_n(\phi_F) = \frac{1}{\pi} \left[\frac{\sin(n+1)\phi_F}{n+1} - \frac{\sin(n-1)\phi_F}{n-1} \right]. \quad (19)$$

The response function $\hat{\chi}_n$ of order n has $n-2$ nodes in the band. In particular, the third-order response function $\hat{\chi}_3$ is positive for less than half full band and negative for more than half full band. The fourth-order response function $\hat{\chi}_4$ is negative at the band edges and positive in the band center.

The bond energy Eq. (16) approaches its TB reference value for $n_{\text{max}} \rightarrow \infty$. If the expansion is terminated at $n_{\text{max}} = 4$, the structural trends across the sp -valent elements may still be described [42]. Furthermore, the difference between the bcc and fcc or hcp structure is to lowest order given by the fourth moment, while resolving the much smaller energy difference between fcc and hcp requires six moments ($n_{\text{max}} = 6$) [25,29]. Higher moments are mainly required for a quantitative match of the TB reference energy, and in practice most BOP calculations are performed with $n_{\text{max}} = 9$.

The expansion of the bond energy Eq. (16) may be applied to discuss trends in crystal structure stability. When an expansion coefficient $\sigma^{(n)}$ is negative, a positive value of the response function $\hat{\chi}_{m+2}(\phi_F) - \gamma_0 \hat{\chi}_{m+1}(\phi_F) + \hat{\chi}_m(\phi_F)$ will lower the energy and vice versa. For making contact with the map of local atomic environments, we take the simplest possible fourth moment expansion with $n_{\text{max}} = 4$, $a^{(\infty)} = a^{(0)} = 0$, and $b^{(\infty)} = b^{(1)} = 1$. Then $\sigma^{(1)} = \sigma^{(2)} = 0$, $\sigma^{(3)} = a^{(1)}$, and $\sigma^{(4)} = (a^{(1)})^2 + (b^{(2)})^2 - 1$.

At less than half full band the simple metals take the close-packed structures bcc, hcp, and fcc. These are stabilized over competing structures by large negative values of $a^{(1)}$ and small values of $b^{(2)}$. The details of the ordering from bcc Na over hcp Mg and fcc Al cannot be resolved within the map of local atomic environments as one cannot expect the simple, nearly-free-electron metals to be described well within a simple TB approximation. At half full band the response function $\hat{\chi}_3$ is zero while $\hat{\chi}_4$ is at its maximum and therefore a small value of $b^{(1)}$ is favorable and helps to stabilize the diamond structure. The subtle competition between graphite and the diamond lattice in carbon is not covered by this argument as the comparison of the two structures at identical second moment is not adequate [29,41,43]. Still, graphene is close to diamond in the d - and sp -map. The dimer, which is stabilized for hydrogen with its half full s -orbitals, takes the minimum of $b^{(2)} = 0$ in an s -valent map (not shown).

The transition metals all take close-packed structures, broadly due to the attraction provided by the s -electrons, while the d -electrons determine the details of the crystal structure. In a map that only takes into account the d -valence, we may therefore not expect to find the transition-metal structures at extreme boundaries of the map. Still, the map places them at large absolute values of $a^{(1)}$ and small values of $b^{(2)}$. As expected the bcc structure, which is stabilized by the response function $\hat{\chi}_4$ at the center of the d -band, has a smaller value of $b^{(2)}$ than fcc or hcp, while hcp and fcc show a slightly more negative value for $a^{(1)}$.

The stability of the TCP phases is more involved, and it has been discussed in detail in [37,44]. The TCP phases are stabilized by a combination of average band filling and atomic size mismatch. The two factors are of different relevance in the different TCP phases. As the atoms in the different coordination polyhedra have different second moments, a direct discussion of the stability of the TCP phases based on the map of local atomic environments alone is not possible. We note that the TCP phases show small values of $b^{(2)}$ for the 12-fold coordinated sites, some of them even smaller than bcc, while the sites with higher coordination show large negative values of $a^{(1)}$.

For evaluating the difference in the bond energy between two structures, one needs to take into account that the Fermi level of the two structures will in general be different. A first-order expansion of the bond energy difference between two structures with the same number of valence electrons N_e at identical first and second moment leads to [37,45]

$$\Delta U_{\text{bond}} = 2(2l+1)b^{(\infty)} \sum_{m=3}^{n_{\text{max}}} \Delta \sigma^{(m)} \hat{\chi}_m(\phi_F), \quad (20)$$

where $\Delta\sigma^{(m)}$ corresponds to the difference in the expansion coefficients,

$$\hat{\chi}_m(\phi_F) = \frac{1}{\pi} \left[\frac{2 \sin(m+1)\phi_F}{m(m+2)} - \frac{\sin(m+3)\phi_F}{(m+2)(m+3)} - \frac{\sin(m-1)\phi_F}{m(m-1)} \right], \quad (21)$$

and ϕ_F depends on the number of valence electrons N_e .

For $n_{\max} = 4$ we can now approximate the difference in energy between two structures as

$$\Delta U_{\text{bond}} = 2(2l+1)[\hat{\chi}_3(\phi_F)\Delta a^{(1)} + \hat{\chi}_4(\phi_F)[\Delta(b^{(2)})^2 + \Delta(a^{(1)})^2]], \quad (22)$$

where we estimate $b^{(\infty)} = b^{(1)} = 1$ and $a^{(\infty)} = a^{(1)} = 0$ as before. We see that the difference between two structures in the map of local atomic environments is approximated by a contribution $\Delta a^{(1)}$ that corresponds to the distance between the structures projected on the x axis and a second contribution that corresponds to the square of the distance between two structures in the map of local atomic environments. The relevance of the two contributions for the energy difference is determined by the number of valence electrons through the response functions Eq. (21). Independent of the detailed number of valence electrons, this implies in general that we may expect that the energy difference between pairs of structures increases with the distance of the structures in the map.

B. Trends of structural stability from TB

We evaluate the bond energy within the TB approximation for the set of random structures in Fig. 6(b) by numerical calculations with the BOPFOX program [33]. We choose a canonical d -valent TB model [Eq. (A1)] with a band filling of 4, which is close to the maximum bcc stability [25,37]. The locally averaged bond energy is shown in Fig. 2(a). We observe a smooth increase of the bond energy from bcc, which has the smallest bond energy among all structures, to the linear chain. The overall trend in the map validates our result from Sec. IV that energy differences between two structures increase with their distance in the map. The standard error of the bond energy was obtained from many different random structures that are projected to a given location in the map of local atomic environments, and it is displayed in Fig. 2(b). The standard error is in the order of 1% of the cohesive energy and hence much lower than the range of energy values in the map of local atomic environments. In other words, the two moments-descriptors allow for the separation of crystal structures that have an energy difference that is greater than about 1% of the cohesive energy. This demonstrates that the descriptors of the map of local atomic environments are excellent predictors for structural stability as a direct consequence of the relation between geometric environment and electronic structure provided by the moments theorem, Eq. (2). This makes our moments-descriptors distinctly different from purely geometrical descriptors.

We show the bond energy for an sp -valent TB model [Eq. (A2)] with different band fillings in Fig. 3. The values

for the bond energy were obtained by averaging over many random structures at each position in the map. The values of the atomic recursion coefficients differ from those obtained for the d -valent TB model, however many features of the d -valent map of local atomic environments are still present in the sp -valent map. As the dimer configuration may be a stable configuration for sp -elements [32], it is an important feature of the sp -valent map that it positions the dimer apart from the other crystal structures. For all band fillings we obtain smooth energy surfaces. As expected at half full band, the diamond structure has the lowest bond energy. For low band fillings, the stability is shifted toward the close-packed phases, while at higher band fillings more open structures are favored [42].

C. Trends of structural stability from DFT

The $4d$ and $5d$ transition metals Mo and W may be described using a band filling of approximately four d -valence electrons; cf. the TB calculations in Sec. IV B [37,46]. To compare to the TB predictions, we performed DFT calculations for Mo for two-atom random structures with both atomic positions occupied by Mo atoms. Here an evaluation of the approximately 90 000 structures that we evaluated for TB was computationally too demanding and we selected a subset of the random structures using the following strategy: The atomic volume of each atom with normalized second moment $\mu^{(2)} = 1$ may be interpreted as a measure for the homogeneity of its atomic surrounding, where a small normalized atomic volume indicates a homogeneous atomic surrounding with equidistant bond lengths. We select from our set of two-atom random structures a subset of 521 structures with small normalized volume that homogeneously covers the existence region of the two-atom cells. For these structures we calculated the DFT equilibrium volume, energy, and bulk modulus with fixed cell shape and atomic positions. We performed spin-polarized DFT calculations using the VASP software [47–49] with the projector augmented-wave method (PAW) [50] with 14 valence electrons (Mo_sv) for molybdenum, and we employ the generalized gradient approximations (GGA) [51] to the exchange correlation potential. The calculations were performed with a plane-wave cutoff energy of 500 eV and Monkhorst-Pack [52] \mathbf{k} -point meshes with linear density not more than 0.1 \AA^{-1} . The equilibrium energy E_0 , volume V_0 , and bulk modulus B_0 were then obtained by fitting energy volume curves with volume scalings of $\pm 10\%$ to the Birch-Murnaghan equation of state. The results are shown in Fig. 4. We observe that the overall trend of the DFT equilibrium energy for Mo [Fig. 4(a)] is qualitatively captured by the bond energy of the corresponding TB calculations at $N_e = 4$ [Fig. 2(a)]. The lowest energy is taken by bcc and the energy increases with distance in the map of local atomic environments. The bcc structure also takes the smallest equilibrium volume. The bulk modulus is smooth across the map of local atomic environments and largest for bcc. The scattering of the results, in particular at the envelopes of the existence region, is an artifact of the relatively smaller number of random structures that we employed in our DFT calculations [see Fig. 6(b)].

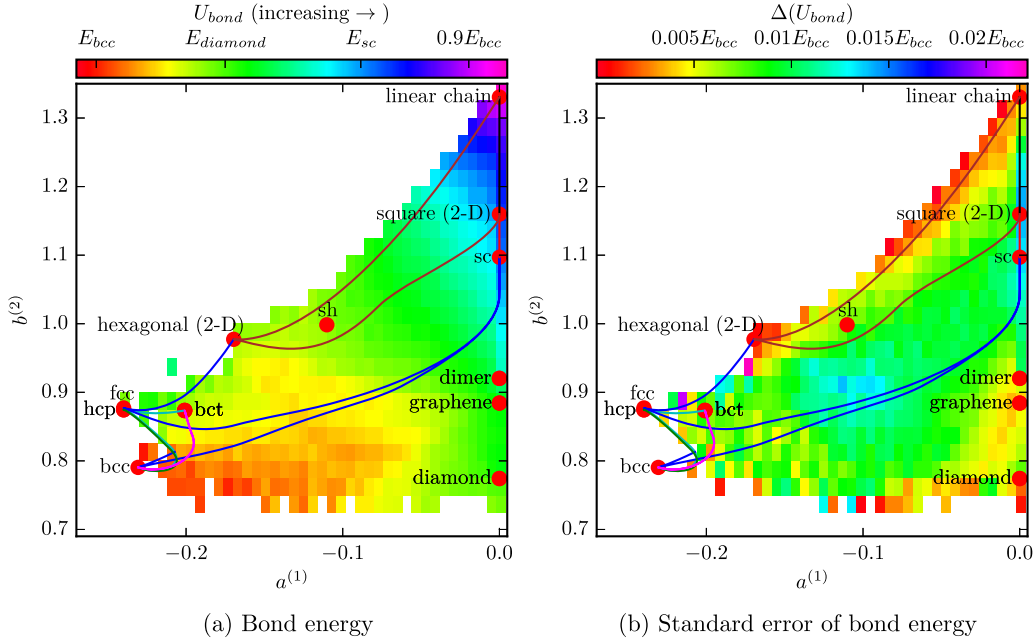


FIG. 2. Analysis of bond energy [Eq. (15)] of two-atom random structures from the canonical d -valent TB model evaluated for a band filling of $N_e = 4$ in the d -valent map of local atomic environments. The left figure shows the averaged bond energy, and the right figure shows the related standard error that is calculated from different random structures at the same position of the map. Lines correspond to transformation paths introduced in Fig. 1.

V. OUTLOOK

The moments-descriptors use the moments theorem to provide a direct link between the local atomic structure and the local electronic structure that determines the binding energy. This link is maintained in a 2D descriptor space, as we demonstrate analytically for the BOPs and numerically for TB and DFT calculations. Therefore, we expect that our map of local atomic environments will prove useful in applications that relate atomic structure and binding energy.

One potential application is the classification of individual atoms in atomistic simulations like, e.g., molecular dynamics.

The typically very large number of atoms in such simulations hinders manual analysis and requires tools for automated identification of processes like nucleation, phase transformation, or dislocation movement. The computation of the coordinates in the map of local atomic environments provides a straightforward approach to identify atoms with similar atomic environment and to assign atoms to a particular crystal structure. The representation with low moments ensures that this computation is feasible also in large-scale simulations.

A second example of a potential application is the development and assessment of empirical or semiempirical interatomic potentials. These potentials are typically developed to

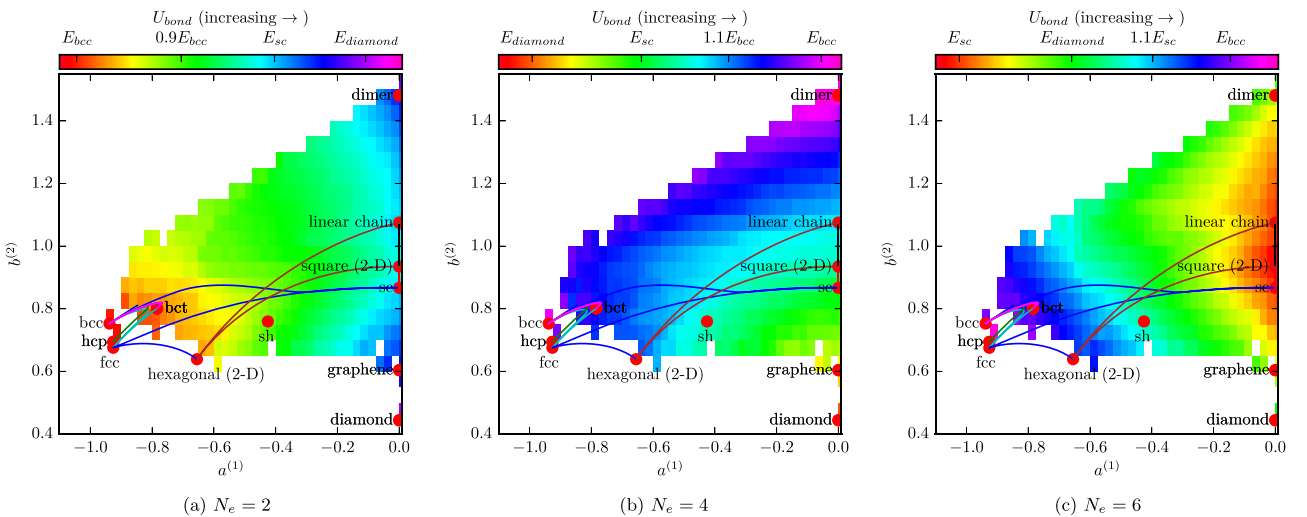


FIG. 3. Bond energy [Eq. (15)] in the sp -valent map of local atomic environments as obtained from the canonical sp -valent TB model for different band fillings. Lines correspond to transformation paths introduced in Fig. 1.

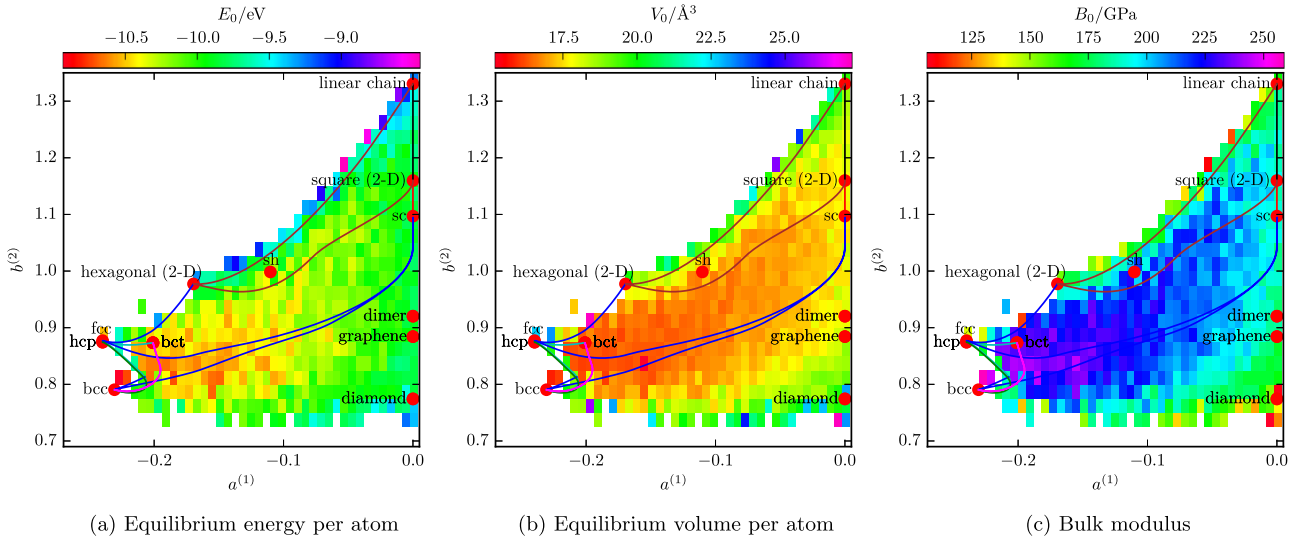


FIG. 4. DFT calculations of equilibrium energy (left), volume (middle), and bulk modulus (right) for a set of random structures with two atomic sites, both occupied by Mo atoms in the d -valent map of local atomic environments. Lines correspond to transformation paths introduced in Fig. 1. The trend of equilibrium energy for Mo obtained by DFT (left) is captured by the bond energy of the corresponding TB calculations at $N_e = 4$ [Fig. 2(a)].

describe the binding energy of a set of reference structures but often exhibit limited transferability to other structures. The challenges are therefore (i) the identification of reference structures in the development of the potential, and (ii) the anticipation of transferability of the interatomic potential. Both aspects can be addressed by the map of local atomic environments as it projects the space of atomic environments on a 2D space, which enables an extensive and homogeneous sampling of atomic environments.

A third potential application is to use the moments-descriptors for a set of atomic environments directly as features for machine-learning to predict, e.g., the DFT formation energy from the atomic structure. The descriptors incorporate domain knowledge of interatomic bond formation, as demonstrated by the smooth DFT data in Fig. 4, and they capture about 99% of the cohesive energy of our TB calculations (cf. Sec. IV B).

VI. CONCLUSION

We introduce moments-descriptors for local atomic environments based on the local electronic density of states. The moments depend on the local atomic environment and determine the bond chemistry. We use the lowest two structure-dependent moments of the electronic density of states as obtained from canonical sp - and d -valent TB models to span a 2D map of local atomic environments. We employ the map of local atomic environments for the discussion of crystal structures. We show that structures with one or two atoms in the primitive cell are bound to specific regions of the map. By making use of the analytic BOP expansion, we argue that the lowest energy structure for a specific material should be found close to the boundaries of these regions. We further show that the energy difference between two structures depends on the distance between the structures in the map, and we carry

out extensive TB and DFT calculations to demonstrate this numerically.

For structures with several inequivalent lattice sites, the map places similar local environments in close proximity, such that the map of local atomic environments may be employed to sample systematically local atomic environments by projecting the local atomic environments to a low-dimensional space. We point out possible applications of this feature of the moments-descriptors for the classification of local atomic environments in molecular-dynamics simulations, for the selection of structure sets for developing and testing interatomic potentials, as well as for the construction of descriptors for machine-learning applications.

ACKNOWLEDGMENTS

We wish to dedicate this paper to the memory of our coauthor Professor David Pettifor CBE FRS, who sadly passed away before the work was completed. A.P.A.S., T.H., and R.D. acknowledge financial support by the German Research Foundation (DFG) through project C1 of the collaborative research center SFB/TR 103. R.D. acknowledges financial support by the German Research Foundation (DFG) through project C2 of the collaborative research center SFB/TR 103. The authors acknowledge Mike Finnis for helpful discussions.

APPENDIX A: DESCRIPTION OF THE CHEMISTRY

In this paper, we restrict our analysis to two different TB models, namely a canonical pure d -model [31],

$$\left. \begin{array}{l} dd\sigma \\ dd\pi \\ dd\delta \end{array} \right\} = \left. \begin{array}{l} -6 \\ 4 \\ -1 \end{array} \right\} \beta(r), \quad (\text{A1})$$

and an sp -model [32] based on Harrison's parametrization [53],

$$\left. \begin{array}{l} ss\sigma \\ sp\sigma \\ pp\sigma \\ pp\pi \end{array} \right\} = \left. \begin{array}{l} -1.00 \\ 1.31 \\ 2.31 \\ -0.76 \end{array} \right\} \beta(r), \quad (\text{A2})$$

with

$$\beta(r) = c/r^5, \quad (\text{A3})$$

where c is a constant. The pure d -model [25,27,36,37,54–56] is often sufficient to describe the elements of the d -block and captures structural trends across the $4d$ and $5d$ transition-metal series [25,27,36,37]. Our sp -model disregards the splitting of the on-site elements [42].

We smoothly force the bond integrals to zero at $r = r_{\text{cut}}$ by multiplying with the cutoff function

$$f_{\text{cut}}(r) = \frac{1}{2} \left\{ \cos \left(\pi \left[\frac{r - (r_{\text{cut}} - d_{\text{cut}})}{d_{\text{cut}}} \right] \right) + 1 \right\}, \quad (\text{A4})$$

where d_{cut} determines the width of the cutoff function. In our calculations, we choose constant values of r_{cut} and d_{cut} , which include second nearest neighbors within the cutoff sphere for the bcc structure, where the second-nearest-neighbor distance is close to the first-nearest-neighbor distance, and we just exclude second nearest neighbors for the simple-cubic structure. This is achieved by choosing $r_{\text{cut}} \approx 1.25r_{\text{nn,fcc}}$ and $d_{\text{cut}} \approx 0.13r_{\text{nn,fcc}}$, where $r_{\text{nn,fcc}}$ is the nearest-neighbor distance of fcc with a normalized second moment according to Eq. (6). Note that the exclusion of second nearest neighbors results in a zero third moment for the simple-cubic structure but not for the fcc and hcp structure, as can be seen in Fig. 1.

APPENDIX B: DESCRIPTION OF TRANSFORMATION PATHS

Transformation paths are continuous deformations of one crystal structure into another. All transformation paths presented in this paper are described by one parameter p changing one structure continuously into the other. Here, we chose transformation paths that are commonly used to test interatomic potentials (tetragonal, orthorhombic, trigonal, hexagonal) [46,57,58], as well as transformation paths (lin.-hex.-sq., lin.-sq., sq.-sc) that we found to correspond to envelopes of the map of local atomic environments. The tetragonal transformation path, also called the Bain path [59], connects bcc with fcc. On further continuation it connects fcc with the special body-centered-tetragonal (bct) structure. This is done by elongating the bcc cell in the [001] direction and compressing it in the [100] and [010] directions to keep the volume fixed.

The primitive cell along the path is given by

$$\begin{aligned} \mathbf{a}_1 &= a(4p)^{-1/3}(-1 \quad 1 \quad p)^T, \\ \mathbf{a}_2 &= a(4p)^{-1/3}(1 \quad -1 \quad p)^T, \\ \mathbf{a}_3 &= a(4p)^{-1/3}(1 \quad 1 \quad -p)^T, \end{aligned}$$

and the atom is located at

$$\mathbf{p}_1 = (0 \quad 0 \quad 0)$$

for all values of p . bcc is taken for $p = 1$, fcc for $p = \sqrt{2}$, and bct for $p = 2^{3/4}$.

The orthorhombic transformation path connects bcc with the same special bct structure, which is reached by the Bain path [35]. Further continuation of the orthorhombic transformation paths leads back to bcc. This is also achieved by an elongation in the [001] direction, however simultaneously a compression in the [110] direction is applied. The primitive cell vectors are therefore

$$\begin{aligned} \mathbf{a}_1 &= 4^{-1/3}a(-1 \quad 1 \quad p^{1/2})^T, \\ \mathbf{a}_2 &= 4^{-1/3}a(1 \quad -1 \quad p^{1/2})^T, \\ \mathbf{a}_3 &= 4^{-1/3}a(p^{-1/2} \quad p^{-1/2} \quad -p^{1/2})^T \end{aligned}$$

and the atom is again located at

$$\mathbf{p}_1 = (0 \quad 0 \quad 0)$$

for all values of p . bcc is taken for $p = 1$, the special bct structure for $p = \sqrt{2}$, and again bcc for $p = 2$.

The trigonal transformation path connects bcc over sc with fcc. Further continuation of the trigonal transformation path connects fcc with the 2D hexagonal lattice. This is obtained by an elongation in the [111] direction and a compression in perpendicular directions to keep the volume fixed. The primitive cell is given by

$$\begin{aligned} \mathbf{a}_1 &= f(p-3 \quad p+2 \quad p+2)^T, \\ \mathbf{a}_2 &= f(p+2 \quad p-3 \quad p+2)^T, \\ \mathbf{a}_3 &= f(p+2 \quad p+2 \quad p-3)^T, \end{aligned}$$

with $f = a[25(3p+1)]^{-1/3}$. The atom remains at the origin again,

$$\mathbf{p}_1 = (0 \quad 0 \quad 0).$$

bcc is taken for $p = 1$, sc for $p = 2$, fcc for $p = 4$, and the 2D hexagonal lattice for $p \rightarrow \infty$.

The bcc to hcp transformation cannot be obtained by a simple deformation of the cell. However, the atoms also have to change their relative positions [58,60]. The hexagonal transformation path deforms bcc simultaneously in the $[\bar{1}10]$, [110], and [001] directions. The cell vectors are explicitly given by

$$\begin{aligned} \mathbf{a}_1 &= 2^{-1/3}af_1(-1 \quad 1 \quad 0)^T, \\ \mathbf{a}_2 &= 2^{-1/3}af_2(0 \quad 0 \quad 1)^T, \\ \mathbf{a}_3 &= 2^{-1/3}a(f_1f_2)^{-1}(1 \quad 1 \quad 0)^T, \end{aligned}$$

with

$$\begin{aligned} f_1 &= 1 + \alpha_1(1-p), \\ f_2 &= 1 + \alpha_2(1-p), \end{aligned}$$

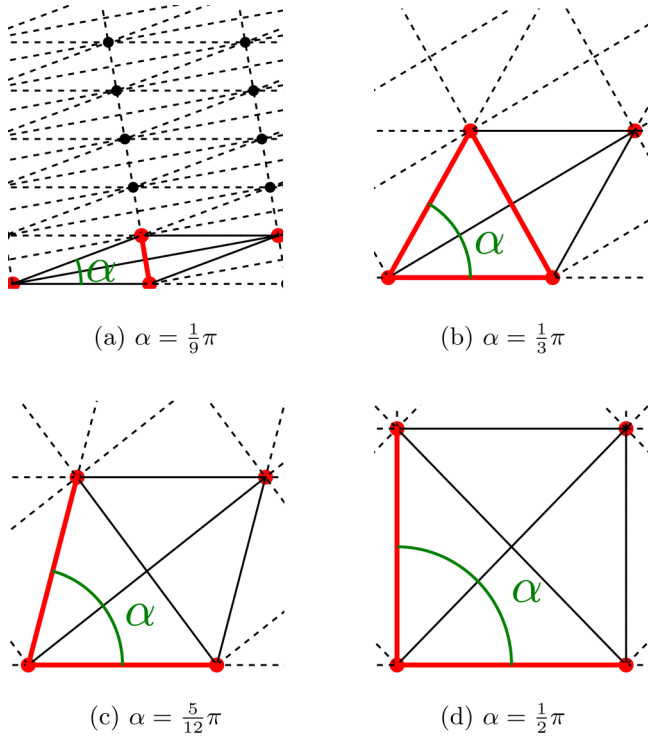


FIG. 5. Transformation path connecting the linear chain with the square lattice over the hexagonal lattice. The shortest bond length is marked in red.

and

$$\alpha_1 = (1 - 2^{1/6}\sqrt{1.5})/(\sqrt{2} - 1),$$

$$\alpha_2 = (1 - 2^{1/6})/(\sqrt{2} - 1).$$

Together with this deformation, alternate (110) planes have to be shuffled in the $\pm[110]$ direction. We follow the choice of Ref. [58] and choose

$$s = \frac{2^{-1/6}(p-1)}{4\sqrt{6}(\sqrt{2}-1)f_1}$$

as the shuffling factor. The atomic positions in the direct coordinate system are given by

$$\mathbf{p}_1 = (s \quad 0 \quad 0),$$

$$\mathbf{p}_2 = (0.5 + s \quad 0.5 \quad 0),$$

$$\mathbf{p}_3 = (-s \quad 0.5 \quad 0.5),$$

$$\mathbf{p}_4 = (0.5 - s \quad 0 \quad 0.5).$$

bcc is taken for $p = 1$ and hcp for $p = \sqrt{2}$.

The linear chain can be connected with the square lattice over the hexagonal lattice as illustrated in Fig. 5 (lin.-hex.-sq.). The cell vectors of the 2D cell are given by

$$\mathbf{a}_1 = a \cos(p)^{-1/2} (1 \quad 0)^T,$$

$$\mathbf{a}_2 = a \cos(p)^{-1/2} (\cos(p) \quad \sin(p))^T.$$

The atom remains at position

$$\mathbf{p}_1 = (0 \quad 0)$$

TABLE I. Selection of common TCP phases and χ -phase ordered by increasing average coordination number. For each coordination number, a list with the number of inequivalent Wyckoff sites is provided.

	CN12	CN13	CN14	CN15	CN16	$\langle \text{CN} \rangle$
χ	12	12			1,4	13.10
C14	2, 6				4	13.33
C15	4				2	13.33
C36	4, 6, 6				4, 4	13.33
μ	1,6		2	2	2	13.38
M	4, 4, 4, 8, 8		4, 4	4, 4	4, 4	13.38
R	1, 2, 6, 6, 6, 6		6, 6	6	2, 6	13.40
δ	4, 4, 4, 4, 4, 4		4, 4, 4, 4, 4	4, 4	4	13.43
P	4, 4, 4, 4, 8		4, 4, 4, 8	4, 4	4	13.43
Z	3		2	2		13.43
A15	2		6			13.50

for all values of p . The square lattice is taken for $p = \pi/2$, the 2D hexagonal lattice for $p = \pi/3$, and the linear chain for $p \rightarrow 0$.

The linear chain can also be directly connected with the 2D square lattice by bringing linear chains from infinite separations together until the linear chains are separated by a distance equal to the nearest-neighbor distance of the linear chain (lin.-sq.).

Similarly, the 2D square lattice can be connected to the simple-cubic structure by bringing square lattices from infinite separations together until the square lattices are separated by a distance equal to the nearest-neighbor distance of the square lattice (sq.-sc).

APPENDIX C: TOPOLOGICALLY CLOSE-PACKED PHASES

Topologically close-packed (TCP) phases consist of coordination polyhedra, which have only triangular faces. The atoms in the TCP phases have coordination numbers 12, 14, 15, or 16. For a selection of common TCP phases the numbers of atoms with inequivalent Wyckoff positions are listed in Table I. As in previous works [27,37,44], we included the χ -phase in the comparison, although it is not a regular TCP phase in the crystallographic sense due to atoms with coordination number 13.

APPENDIX D: RANDOM STRUCTURES

With random structures we refer to structures generated by randomly choosing their primitive cell and their atomic positions in the primitive cell. The primitive cell is described by the lattice vectors $\mathbf{a} = a\mathbf{e}_a$, $\mathbf{b} = b\mathbf{e}_b$, $\mathbf{c} = c\mathbf{e}_c$. The angle between \mathbf{b} and \mathbf{c} is named α , the angle between \mathbf{a} and \mathbf{c} is named β , and the angle between \mathbf{a} and \mathbf{b} is named γ .

The structure generation is done as follows:

(i) Randomly generate three values $a \leq b \leq c$, with $b/a \leq 3$ and $c/a \leq 3$.

(ii) Randomly generate angles α, β, γ in a range between 0 and π under the condition that the volume is larger than zero [61].

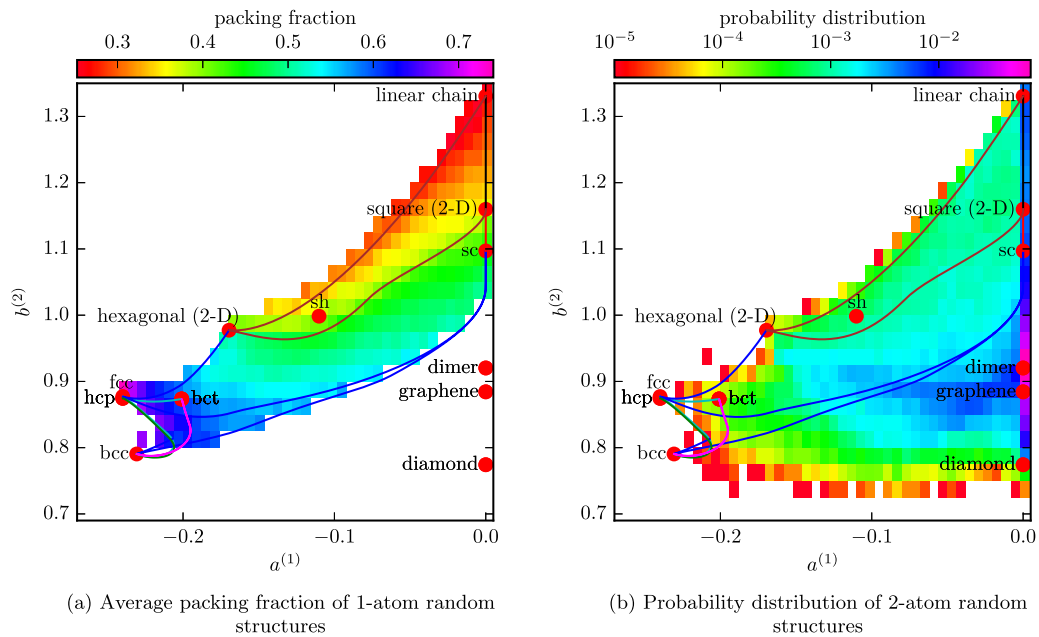


FIG. 6. Random structures with one or two atoms in the primitive cell in a d -valent map of local atomic environments. The left figure shows the average packing fraction that is obtained for the random structures with one atom in the primitive cell. The right figure shows the probability distribution of the random structures with two atoms in the primitive cell when the structures are generated according to the algorithm outlined in Appendix D. Lines correspond to transformation paths introduced in Fig. 1.

(iii) Place the first atom at the origin and place further atoms randomly in the primitive cell.

(iv) Even though we generate primitive cells with a finite volume, the generated structure may be effectively 2D due to the finite number of bonds, which we obtain due to the choice of the cutoff r_{cut} of our bond integrals β . We exclude those structures.

In Fig. 6(a) we characterize the set of one-atom random structures in terms of the averaged packing fraction and observe a smooth trend across the map of local atomic environments. The packing fraction is lowest for those 3D structures that are close to the linear chain in the map. The averaged packing fraction increases toward the bottom and the left of the map of local atomic environments and takes its maximum

value close to fcc and hcp, which have the highest possible value [62].

The random structures do not cover the map of local atomic environments homogeneously. In Fig. 6(b) we show the probability for generating a structure in a particular location of the map of local atomic environments with our algorithm. The probability distribution was obtained from a set of approximately 90 000 random structures with two atoms in the primitive cell. It is significantly more likely to generate an open structure with $a^{(1)} = 0$ than a close-packed structure close to fcc and hcp. It can be seen that with this method it is very unlikely to generate structures that are similar to highly symmetric structures. However, it ensures that we do not bias the random structures toward any reference structures.

-
- [1] P. J. Steinhardt, D. R. Nelson, and M. Ronchetti, *Phys. Rev. B* **28**, 784 (1983).
- [2] W. Lechner and C. Dellago, *J. Chem. Phys.* **129**, 114707 (2008).
- [3] A. P. Bartók, M. C. Payne, R. Kondor, and G. Csányi, *Phys. Rev. Lett.* **104**, 136403 (2010).
- [4] A. P. Bartók, R. Kondor, and G. Csányi, *Phys. Rev. B* **87**, 184115 (2013).
- [5] J. Behler, *J. Chem. Phys.* **134**, 074106 (2011).
- [6] N. Artrith, T. Morawietz, and J. Behler, *Phys. Rev. B* **83**, 153101 (2011).
- [7] S. Hajinazar, J. Shao, and A. N. Kolmogorov, *Phys. Rev. B* **95**, 014114 (2017).
- [8] M. Rupp, A. Tkatchenko, K.-R. Müller, and O. A. von Lilienfeld, *Phys. Rev. Lett.* **108**, 058301 (2012).
- [9] O. A. von Lilienfeld, R. Ramakrishnan, M. Rupp, and A. Knoll, *Int. J. Quantum Chem.* **115**, 1084 (2015).
- [10] K. Hansen, F. Biegler, R. Ramakrishnan, W. Pronobis, O. A. von Lilienfeld, K.-R. Müller, and A. Tkatchenko, *J. Phys. Chem. Lett.* **6**, 2326 (2015).
- [11] A. F. Bialon, T. Hammerschmidt, and R. Drautz, *Chem. Mater.* **28**, 2550 (2016).
- [12] L. M. Ghiringhelli, J. Vybiral, S. V. Levchenko, C. Draxl, and M. Scheffler, *Phys. Rev. Lett.* **114**, 105503 (2015).
- [13] Y. Saad, D. Gao, T. Ngo, S. Bobbitt, J. R. Chelikowsky, and W. Andreoni, *Phys. Rev. B* **85**, 104104 (2012).
- [14] K. T. Schütt, H. Glawe, F. Brockherde, A. Sanna, K. R. Müller, and E. K. U. Gross, *Phys. Rev. B* **89**, 205118 (2014).
- [15] O. Isayev, D. Fourches, E. N. Muratov, C. Oses, K. Rasch, A. Tropsha, and S. Curtarolo, *Chem. Mater.* **27**, 735 (2015).
- [16] F. Cyrot-Lackmann, *Adv. Phys.* **16**, 393 (1967).
- [17] S. Goedecker and L. Colombo, *Phys. Rev. Lett.* **73**, 122 (1994).
- [18] S. Goedecker and M. Teter, *Phys. Rev. B* **51**, 9455 (1995).
- [19] D. G. Pettifor, *Phys. Rev. Lett.* **63**, 2480 (1989).

- [20] M. Aoki and D. G. Pettifor, *Int. J. Mod. Phys. B* **07**, 299 (1993).
- [21] M. Aoki, *Phys. Rev. Lett.* **71**, 3842 (1993).
- [22] A. P. Horsfield, A. M. Bratkovsky, M. Fearn, D. G. Pettifor, and M. Aoki, *Phys. Rev. B* **53**, 12694 (1996).
- [23] R. Silver, H. Roeder, A. Voter, and J. Kress, *J. Comput. Phys.* **124**, 115 (1996).
- [24] A. F. Voter, J. D. Kress, and R. N. Silver, *Phys. Rev. B* **53**, 12733 (1996).
- [25] R. Drautz and D. G. Pettifor, *Phys. Rev. B* **74**, 174117 (2006).
- [26] R. Drautz and D. G. Pettifor, *Phys. Rev. B* **84**, 214114 (2011).
- [27] T. Hammerschmidt, A. N. Ladines, J. Koßmann, and R. Drautz, *Crystals* **6**, 18 (2016).
- [28] R. Haydock, *Comput. Phys. Commun.* **20**, 11 (1980).
- [29] D. G. Pettifor, *Bonding and Structure of Molecules and Solids* (Oxford University Press, Oxford, 1995).
- [30] J. Shohat, *Biometrika* **21**, 361 (1929).
- [31] O. K. Andersen, W. Klose, and H. Nohl, *Phys. Rev. B* **17**, 1209 (1978).
- [32] J. C. Cressoni and D. G. Pettifor, *J. Phys.: Condens. Matter* **3**, 495 (1991).
- [33] T. Hammerschmidt, B. Seiser, M. E. Ford, A. N. Ladines, N. Wang, J. Jenke, Y. Lysogorskiy, C. Teijeiro, M. Mrovec, M. Čák, E. R. Margine, D. G. Pettifor, and R. Drautz, *Comput. Phys. Commun.* (2018), doi: 10.1016/j.cpc.2018.08.013.
- [34] A better differentiation between fcc and hcp can easily be set up by using higher recursion coefficients for the axes, such as $a^{(2)}$ and $b^{(3)}$. However, the lowest moment contributions $a^{(1)}$ and $b^{(2)}$ are most important for a general structural differentiation, such that a higher-dimensional map would be required for a general structural differentiation [27].
- [35] W. Luo, D. Roundy, M. L. Cohen, and J. W. Morris, *Phys. Rev. B* **66**, 094110 (2002).
- [36] T. Hammerschmidt, B. Seiser, R. Drautz, and D. G. Pettifor, Modelling topologically close-packed phases in superalloys: Valence-dependent bond-order potentials based on ab-initio calculations, in *Superalloys* (The Metals, Minerals and Materials Society, Warrendale, PA, 2008), pp. 847–853.
- [37] B. Seiser, T. Hammerschmidt, A. N. Kolmogorov, R. Drautz, and D. G. Pettifor, *Phys. Rev. B* **83**, 224116 (2011).
- [38] A. P. Sutton, M. W. Finnis, D. G. Pettifor, and Y. Ohta, *J. Phys. C* **21**, 35 (1988).
- [39] R. Drautz, T. Hammerschmidt, M. Čák, and D. G. Pettifor, *Modell. Simul. Mater. Sci. Eng.* **23**, 074004 (2015).
- [40] D. G. Pettifor, *J. Phys. C* **19**, 285 (1986).
- [41] We note that the assumption Eq. (13) has its limitations and is not always valid. For example, the χ -phase structure of Mn is stabilized over hcp that is taken by the isoelectronic Tc or Re by a softer repulsion with an exponent that is smaller than 2 as Mn does not have d -states in the core [43]. The same holds for carbon, where graphite is stabilized over the diamond structure by the same mechanism [29].
- [42] R. Drautz, D. A. Murdick, D. Nguyen-Manh, X. Zhou, H. N. G. Wadley, and D. G. Pettifor, *Phys. Rev. B* **72**, 144105 (2005).
- [43] J. F. Drain, R. Drautz, and D. G. Pettifor, *Phys. Rev. B* **89**, 134102 (2014).
- [44] T. Hammerschmidt, A. F. Bialon, D. G. Pettifor, and R. Drautz, *New J. Phys.* **15**, 115016 (2013).
- [45] P. Turchi and F. Ducastelle, in *The Recursion Method and Its Applications: Proceedings of the Conference, Imperial College, London*, edited by D. G. Pettifor and D. L. Weaire (Springer, Berlin, 1987), pp. 104–119.
- [46] M. Čák, T. Hammerschmidt, J. Rogal, V. Vitek, and R. Drautz, *J. Phys.: Condens. Matter* **26**, 195501 (2014).
- [47] G. Kresse and J. Hafner, *Phys. Rev. B* **47**, 558 (1993).
- [48] G. Kresse and J. Furthmüller, *Comput. Mater. Sci.* **6**, 15 (1996).
- [49] G. Kresse and J. Furthmüller, *Phys. Rev. B* **54**, 11169 (1996).
- [50] P. E. Blöchl, O. Jepsen, and O. K. Andersen, *Phys. Rev. B* **49**, 16223 (1994).
- [51] J. P. Perdew, K. Burke, and M. Ernzerhof, *Phys. Rev. Lett.* **77**, 3865 (1996).
- [52] H. J. Monkhorst and J. D. Pack, *Phys. Rev. B* **13**, 5188 (1976).
- [53] W. A. Harrison, *Electronic Structure and Properties of Solids* (Freeman, San Francisco, 1980).
- [54] A. Urban, M. Reese, M. Mrovec, C. Elsässer, and B. Meyer, *Phys. Rev. B* **84**, 155119 (2011).
- [55] G. K. H. Madsen, E. J. McEniry, and R. Drautz, *Phys. Rev. B* **83**, 184119 (2011).
- [56] E. J. McEniry, G. K. H. Madsen, J. F. Drain, and R. Drautz, *J. Phys.: Condens. Matter* **23**, 276004 (2011).
- [57] Y. S. Lin, M. Mrovec, and V. Vitek, *Phys. Rev. B* **93**, 214107 (2016).
- [58] V. Paidar, L. G. Wang, M. Sob, and V. Vitek, *Modell. Simul. Mater. Sci. Eng.* **7**, 369 (1999).
- [59] E. C. Bain, *Trans. Am. Inst. Min. Metall. Eng.* **70**, 25 (1924).
- [60] M. Friák and M. Šob, *Phys. Rev. B* **77**, 174117 (2008).
- [61] J. Foadi and G. Evans, *Acta Crystallogr. Sect. A* **67**, 93 (2011).
- [62] T. C. Hales, *Ann. Math.* **162**, 1065 (2005).